## **Green Chemistry**



PAPER View Article Online
View Journal | View Issue



**Cite this:** *Green Chem.*, 2017, **19**, 2826

# Informing rational design of graphene oxide through surface chemistry manipulations: properties governing electrochemical and biological activities†

Yan Wang 📵 and Leanne M. Gilbertson 📵 \*

It is increasingly realized that rational design is critical to advance potential applications and proactively preclude adverse consequences of carbon nanomaterials (CNMs). Central to this approach is the establishment of parametric relationships that correlate material properties to both their functional performance and inherent hazard. This work aims to decouple the causative mechanisms of material structure and surface chemistry as it relates to the electrochemical and biological activities of graphene oxide (GO). The results are evaluated in the context of established relationships between surface chemistry and oxygen functionalized multi-walled carbon nanotubes (O-MWCNTs), a carbon allotrope. Systematic manipulation of GO surface chemistry is achieved through thermal annealing (under inert conditions, 200-900 °C). To further elucidate the contribution of several properties, chemical reduction was also used as an approach to differentially modify the surface chemistry. Physicochemical properties of GO and reduced GO (rGO) samples were comprehensively characterized using multiple techniques (AFM, TGA, XPS, ATR-FTIR, Raman, and DLS). The results indicate that surface chemistry is a viable design handle to control both activities. Rather than a single direct property (i.e., relative presence of carbonyl-containing mojeties), it is a balance of multiple consequential properties, (extent of dispersion, defect density, and electrical conductivity) in combination with the relative presence of carbonyl moieties that synergistically contribute to electrochemical and biological activities. The identification of these governing physicochemical properties aims to inform the establishment of design parameters to guide the rational and safe design of CNMs.

Received 13th January 2017, Accepted 23rd March 2017 DOI: 10.1039/c7gc00159b

rsc.li/greenchem

#### 1. Introduction

Rational chemical design motivated by green chemistry has stimulated an impressive body of work in which the function and hazard of chemicals are decoupled at the molecular level. At the core of this rational design approach is the identification of physicochemical properties – ideally those that can be manipulated – that govern the function and hazard. For chemicals, correlations between their structure, physicochemical properties and toxicity manifest as Quantitative Structure–Activity (and Toxicity) Relationships (QSAR and QSTR), which guide chemists in the molecular design process to reduce the inherent hazard through chemical structure and property manipulations. This 'design of

Department of Civil and Environmental Engineering, University of Pittsburgh, Pittsburgh, PA 15261, USA. E-mail: leanne.gilbertson@pitt.edu;
Tel: +1 (412) 624-1683

†Electronic supplementary information (ESI) available. See DOI: 10.1039/c7gc00159b

safer chemicals' approach and the unfortunate history that motivated its emergence, underlines the critical need for proactive development of design guidelines for new and emerging chemicals. Engineered nanomaterials (ENMs) are one such class of chemicals that present tangible benefits and market penetration<sup>5</sup> with potential concomitant adverse environmental and human health consequences.

One- and two-dimensional configurations of carbon nanomaterials (CNMs), including carbon nanotubes (CNTs) and graphene, have captured the attention of researchers due to their unique physicochemical properties. In particular, CNM exceptional electronic properties have advanced a wide range of applications in electronic and electrochemical devices, energy conversion and storage, and sensors. <sup>6-11</sup> The estimated global market of graphene-based products alone are estimated to grow from \$1.5 million in 2015 to \$310.4 million in 2020. <sup>5</sup> Given their versatile applications and demonstrated significant magnitudes of (cyto)toxicity, <sup>12-19</sup> concerns have been raised regarding the potential for these materials to impart adverse consequences in the event of the unintended release to the

environment and human exposure.20-22 The balance of promoting the use of CNMs in promising applications while preventing unintended consequences presents a critical challenge that motivates a rational design approach for sustainable development of promising CNM-enabled products. Similar to chemicals, this balance can be met through the establishment of relationships that relate specific structure and/or material properties to the functional performance and inherent hazard.23 Interestingly, the electron transport and specific surface functional moieties of CNMs have been shown to be important for both electrochemical and activities. 12,18,24-28 These properties can be manipulated through their dependence on material structure and surface chemistry. Decoupling the causative mechanism of material structure and surface chemistry in relation to electrochemical and biological activities is thus a critical step toward rational and sustainable CNM design.

Gilbertson et al. previously demonstrated the ability to control the electrochemical (a desired function) and biological activities of oxygen functionalized multi-walled carbon nanotubes (O-MWCNTs) by manipulating their surface chemistry. 19,24 In that work, the relative presence of carbonyl moieties was identified as the governing parameter, influencing both biological and electrochemical activities. The research presented herein, aims to determine whether, (i) surface chemistry alone governs electrochemical and biological activities of all CNMs, or (ii) the activities of CNMs are driven by unique material properties (e.g., structure, electronic). Given the chemical similarity and distinct structure of CNTs and graphene, the surface chemistry of graphene is manipulated in the same way as the previously studied O-MWCNTs (i.e., oxygen functionalization) to produce a systematically modified graphene oxide (GO) material suite. The comparison of governing physicochemical properties on the corresponding electrochemical and biological activities within these two CNM allotropes will thus inform the potential establishment of guidelines for the controlled and tailored design of CNMs.

Like graphene, GO consists of a single atomic plane of carbon arranged in a network of sp<sup>2</sup>-carbons decorated with different oxygen moieties, including epoxide and hydroxyl groups on the basal planes and carboxylic and carbonyl groups at the edges.<sup>29,30</sup> Surface functionalization introduces a hybrid structure consisting of variable sp<sup>2</sup> and sp<sup>3</sup> carbon bonding schemes.<sup>29,30</sup> The balance of sp<sup>2</sup>-sp<sup>3</sup> carbons directly influences the electronic properties (*e.g.*, conductivity) thus, presenting an opportunity to tailor these properties of graphene by manipulating specific oxygen groups of GO.<sup>31-33</sup>

A critical underpinning of the proposed rational design approach is the establishment of a systematically modified and comprehensively characterized material suite, which further enables movement beyond the reported inconsistencies of graphene and GO biological activity (detailed discussion is included in the ESI and data compiled in Table S1†). Two approaches, thermal annealing and chemical reagent reduction, were used in this work to prepare a series of reduced GO (rGO) samples from the same starting GO.

Thermally reduced GO samples with varying surface chemistries were obtained through selective reduction of oxygen functional groups - based on their thermal stability on carbon surfaces<sup>34</sup> - by varying the maximum temperature from 200 to 900 °C. One chemically reduced GO sample was prepared through deoxygenation with sodium borohydride (NaBH<sub>4</sub>). Comprehensive characterization is necessary to establish governing relationships between specific material properties and the desired function and hazard outcomes. In addition to standard approaches to characterize the structure, physical and chemical properties, significant attention is given in this study to the biological and electrochemical activities, which are characterized using independent approaches. The trends in electrochemical and biological activities are correlated with the specific GO/rGO physicochemical properties, including extent of dispersion (measured as aggregate size and distribution), defect density, electrical conductivity, and the relative presence of different oxygen functional groups. The balance of these contributing properties is discussed as it relates to the identified trends in the measured electrochemical and biological activity endpoints.

## 2. Experimental

## 2.1 Preparation of graphene oxide and reduced graphene oxide material suite

Graphene oxide (GO). Powdered single layer GO (~99% purity), synthesized using the modified Hummer's method, was purchased from ACS Materials LLC (Medford, MA, USA, product no. GNO1P005), and used as-received (ARGO).

Reduced GO (rGO) samples *via* thermal annealing. Systematic surface modified GO was prepared by a thermal treatment under helium gas flow in a tube furnace (Thermo Scientific Lindberg/Blue M TF55035A-1) with custom-built quartz tube at increasing maximum temperatures 200, 400, 600 and 900 °C. The ARGO was added to the quartz tube and heated at a rate of 5 °C min<sup>-1</sup> to the maximum temperature, held for 30 min, and then left to cool at room temperature (under He flow). These thermally reduced GO samples are henceforth referred to as TGO200, TGO400, TGO600, and TGO900, respectively.

Chemically reduced GO. The chemically reduced GO (CGO) sample was prepared using the method of Gao *et al.*<sup>35</sup> Briefly, 100 mg of ARGO was dispersed in 100 mL deionized water by 30 min bath sonication (VWR Aquasonic 150 T). After sonication, the pH of the ARGO dispersion was adjusted to 9.5 using 5 wt% sodium carbonate (Na<sub>2</sub>CO<sub>3</sub>). 20 mL of 40 g L<sup>-1</sup> NaBH<sub>4</sub> was added and the mixture was heated to 80 °C under constant stirring for 1 hour. The final CGO sample was isolated by filtration, rinsed ten times with 250 mL deionized water, and dried in a vacuum desiccator with phosphorous pentoxide for 48 hours. This chemical reduction method was chosen because it avoids using a hazardous reducing reagent (*e.g.*, hydrazine) and further, precludes the incorporation of functional groups, such as C–N groups with hydrazine

**Paper Green Chemistry** 

reduction, limiting the potential for impurities in the final product. 35,36 Since the CGO sample was prepared using NaBH<sub>4</sub> and boron-doped CNMs are known efficient electrocatalysts, 37,38 the potential for boron to confound the electrochemical activity of CGO was investigated by XPS (Fig. S1†). The results confirm the absence of boron in the CGO sample.

#### 2.2 Characterization of the prepared samples

ARGO, TGOs, and CGO were characterized using atomic force microscopy (AFM, to evaluate potential changes in the lateral dimension and sheet height before and after reductive treatments), thermogravimetric analysis (TGA, to determine the thermal stability and purity of ARGO), X-ray photoelectron spectroscopy (XPS, to quantify the surface chemistry and distribution of functional groups via C-O bonding schemes), attenuated total reflectance-Fourier transform infrared spectroscopy (ATR-FTIR, to confirm the changes in surface chemistry as a complementary technique to XPS), and Raman spectroscopy (to determine the degree of disorder or defect density and the crystallite size). The electrical conductivity of GO/rGO samples was determined using the four-point technique. The methodological details of these techniques are described in the ESI.†

#### 2.3 Biological activity using the oxidation of glutathione (GSH) assav

GSH was used in this study to evaluate the relative biological activity of the differentially treated GO/rGO samples following a previously described method. 13,19,39 Method details can be found in the ESI.† Statistical analysis of the results included two-sample t test with a 95% confidence interval (CI) and a 0.05 level of significance (P value).

#### 2.4 Electrochemical measurements

Rotating ring-disk electrode (RRDE) technique was employed for electrochemical characterization of the prepared GO/rGO samples using a WaveDriver 20 Bipotentiostat (PINE Research Instrument, NC, USA) and a PINE modulated speed rotator. The details of the methods for the determination of the kinetic limiting current density ( $J_{\rm K}$ , mA cm<sup>-2</sup>), the electron transfer number (n), the H2O2 yield (H2O2%), and the electroactive surface area of samples (A) can be found in the ESI.†

#### 3. Results and discussion

### Probing the lateral size and the height of GO/rGO samples by AFM imaging

AFM imaging was carried out to, (i) confirm the single layer conformation of ARGO, and (ii) reveal any changes in lateral size and height of the samples upon reductive treatments (Fig. S2†). The isolated ARGO flakes are found to have an average sheet height of 1.34 nm, indicating that ARGO sheets are single-layered. 40,41 The average sheet heights of TGO600 and CGO are around 2.55  $\pm$  1.74 and 4.46  $\pm$  3.62 nm, respectively. The individual single-layer sheets still exist in these two rGO samples, however, disordered clusters can be observed and form by random aggregation of these single-layer sheets in accordance with other studies. 42,43 Thus, the rGO samples include a mix of single- and multi-layer sheets as well as aggregated rGO sheets. In addition, the average lateral size of ARGO, TGO600, and CGO were determined to be 186 ± 103, 191  $\pm$  128, and 239  $\pm$  155 nm, respectively, and is based on analysis of approximately 100-150 sheets captured from multiple acquired images (Fig. S2†). Although there is a range in lateral size distributions, the GO/rGO sheets being investigated are smaller than 1 µm.

#### 3.2 Characterizing surface chemistry as a function of thermal and chemical reduction to inform the potential to tailor GO/rGO physicochemical properties

Thermal and chemical reduction processes were explored as mechanisms to control graphene surface chemistry and the potential to serve as a path towards tailoring resultant physicochemical properties. As such, comprehensive characterization of surface chemistry is critical and was characterized using multiple complementary techniques, including TGA, XPS, and ATR-FTIR. The results from each will be discussed in turn as it relates to elucidating distinct GO/rGO surface chemistries.

TGA monitors the sample mass during temperature cycling, and can be evaluated under different gas environments. Here, the sample mass loss was determined under nitrogen (N2) and air to evaluate the thermal stability and the purity of ARGO. The significant mass loss (~40%) observed between 100 and 200 °C under N2 atmosphere (Fig. S3†) is attributed to the release of CO and CO2 from the decomposition of labile oxygen surface groups (e.g., water molecules, epoxides). 44 The systematic mass loss above 200 °C indicates the subsequent loss of more stable oxygen functional groups. 45 Complete oxidation of ARGO occurs around 500 °C under air; over 95% mass loss indicates minimal residue and high purity of ARGO.

XPS was employed to further resolve the reduction in total surface oxygen (C/O atomic ratio in Table 1) and the type of surface oxygen (remaining columns in Table 1) as a function of thermal and chemical reduction. These data are compiled in Table 1 and determined from peak deconvolution of the high-resolution C 1s spectra shown in Fig. 1. The C 1s spectrum of the ARGO exhibits well defined double peaks with sp<sup>2</sup> and sp3 carbon components (~284.8 eV and 287.0 eV, respectively),46 indicating the presence of a large amount of sp3 carbon (i.e., presence of functional groups). After thermal or chemical reduction, the C 1s spectrum shifts to a single sharp peak at sp<sup>2</sup> carbon position owing to the restoration of sp<sup>2</sup> bonding.30 The C/O atomic ratio - the metric commonly used to indicate the relative presence of oxygen functionalization of different oxidized carbon samples - increases, as expected, with maximum annealing temperature (ARGO to TGO900), reaching 5.80 for the sample annealed at 900 °C. The CGO C/O ratio increases from 1.58 (ARGO) to 3.52, which is equivalent

Samples	C:O	% sp <sup>2</sup> carbon	% C-O	% C=O	% СООН
ARGO	$1.58 \pm 0.04$	$36.98 \pm 0.70$	$47.48 \pm 0.92$	$8.74 \pm 0.63$	$6.79 \pm 0.48$
TGO200	$3.04 \pm 0.07$	$68.74 \pm 1.18$	$14.68 \pm 2.21$	$8.48 \pm 0.97$	$8.11 \pm 0.31$
TGO400	$3.52 \pm 0.04$	$73.28 \pm 0.73$	$16.03 \pm 1.51$	$6.91 \pm 0.92$	$3.79 \pm 0.25$
TGO600	$3.68 \pm 0.06$	$76.50 \pm 0.09$	$15.62 \pm 0.32$	$4.74 \pm 0.18$	$3.14 \pm 0.10$
TGO900	$5.80 \pm 0.13$	$86.72 \pm 1.74$	$9.08 \pm 1.71$	$3.21 \pm 0.16$	$1.00 \pm 0.21$
CGO	$3.52 \pm 0.05$	$74.49 \pm 0.39$	$15.67 \pm 0.08$	$5.50 \pm 0.12$	$4.35 \pm 0.32$

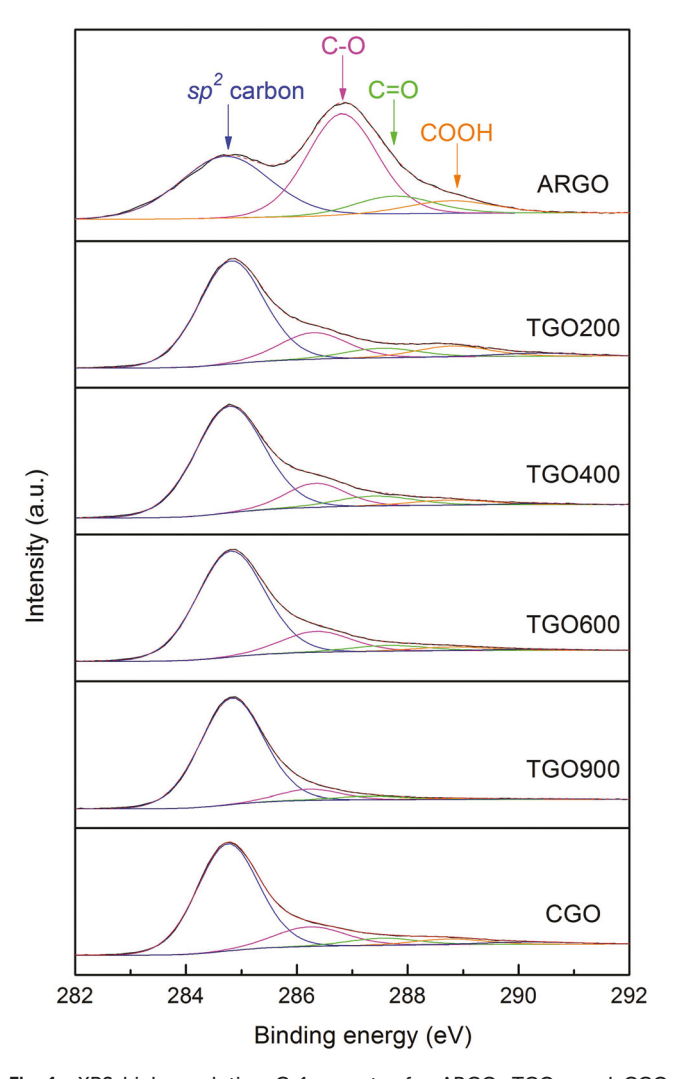


**Fig. 1** XPS high-resolution C 1s spectra for ARGO, TGOs, and CGO. Peak deconvolution was completed using four representative peaks for the sp<sup>2</sup> carbon and the respective C–O bonding schemes as indicated by the different color curves. Three C 1s spectra were collected at different locations of each sample, peak deconvolution was performed for each C 1s spectrum and the average values for four components were compiled in Table 1.

to that of TGO400. The observed increase of the C/O ratio confirms the effective reduction of surface oxygen and the relative extent of reduction for the methods employed.

Peak fitting of the C 1s spectra can further resolve the various carbon-oxygen bonding schemes, including unoxidized sp<sup>2</sup> carbon (~284.8 eV), hydroxyl and epoxide (C-O, ~286.4 eV), carbonyl (C=O, ~287.5 eV), and carboxylic acid (COOH, ~288.8 eV) groups, to provide additional insight into the type of oxygen on the prepared graphene surfaces. The assignment of these four features is in agreement with the previous studies. 30,33,47-49 The sp<sup>2</sup> carbon fraction confirms the degree of reduction, the trend of which should (and does here) coincide with that of the C/O ratio, indicating the restoration of the aromatic (sp<sup>2</sup>) carbon structure. As the electrical properties of CNMs are primarily determined by the  $\pi$  electrons of sp<sup>2</sup> carbon,<sup>50</sup> changes in the sp<sup>2</sup> carbon fraction can significantly influence the GO/rGO reactivity. The percent contribution of C-O (Table 1) indicates it is the major bonding scheme present on ARGO and that upon reduction, the C-O fraction significantly decreases (47.48% for ARGO to 14.68% for TGO200 and 15.67% for CGO). This is attributed to reduction of epoxide groups, which are most abundant on GO30,33,51 and are neither thermally or chemically stable. For TGO900, the relative contribution of the C-O bonding scheme is highest, which may be attributed to the stability of C-OH groups at high temperature, particularly those that are intercalated into interlayers of graphene domains.30,48 Above 200 °C, the C=O and COOH moieties exhibit a steady decrease upon thermal reduction.

The O 1s spectra (Fig. S4†) complement the C 1s spectral observations and trends. There are two primary core-level components of the O 1s spectra, the single-bonded C-O species ( $\sim$ 533 eV) and double-bonded C=O species ( $\sim$ 531 eV).  $^{33,52}$ These two components are clearly visible during reduction processes, and remain in the spectra of the TGO900 and CGO samples. This indicates that both the thermal and chemical reduction methods employed do not completely regenerate pure graphene. Rather, residual oxygen remains on the surface, consistent with the findings from peak deconvolution of C 1s spectra. Combined, the XPS data indicate that thermal and chemical reduction processes, (i) are successful at systematically reducing the total amount of surface oxygen, and (ii) provide an approach to tailor the functional group composition (i.e., relative amount of different groups). ATR-FTIR is a complementary technique to characterize the GO/rGO surface chemistry, particularly shifts in the relative abundance of certain bonding schemes. Data collected for all samples are

**Paper** 

compiled in Fig. S5<sup>†</sup> and are accompanied by discussion of the results that confirm the XPS data trends.

# 3.3 Quantifying defects and restoration of the aromatic carbon domain by Raman spectroscopy

Raman is a widely-used tool to study the crystal structure and examine the degree of disorder or defects in carbonaceous materials. Raman spectra were collected for all samples and are compiled in Fig. S6.† There are two prominent peaks at ~1350 cm<sup>-1</sup> and ~1585 cm<sup>-1</sup>, representative of the D- and G-band, respectively. The D-band arises from the breathing modes of six-membered rings and the intensity indicates the presence of defects. These defects include sp<sup>3</sup> carbons, bondangle or bond-length disorders, edge defects, grain boundaries, vacancies, or even physical defects like holes and wrinkles. 53-55 The G-band originates from the in-plane sp<sup>2</sup> carbon stretching mode of the graphene lattice.<sup>53</sup> In addition, there is a lower magnitude broad bump-like peak observed at high wavenumbers (2400-3250 cm<sup>-1</sup>) that is representative of the 2D region, including several characteristic bands denoted as 2D ( $\sim$ 2700 cm<sup>-1</sup>), D + G ( $\sim$ 2930 cm<sup>-1</sup>), and 2G ( $\sim$ 3170 cm<sup>-1</sup>) bands.54-56 It has been reported that the emergence of the modulated bump in the 2D region indicates the existence of a large amount of defects; this high disorder results in the suppression of the 2D band, reducing its intensity.<sup>56,57</sup> The Raman spectra for all samples present this broad peak at high wavenumbers.

The relative intensity ratio of the D and G band  $(I_{\rm D}/I_{\rm G})$  is a commonly used metric to characterize the level of defects. Further, it can be used to evaluate the crystallite size of the basal planes  $(L_{\rm a})$  and the distance between the defects  $(L_{\rm d})$ . Second An increase in the  $I_{\rm D}/I_{\rm G}$  is commonly observed upon reduction of GO, S4,55,61-63 and is in agreement with results presented here as shown in Fig. 2 (left axis). Both reduction

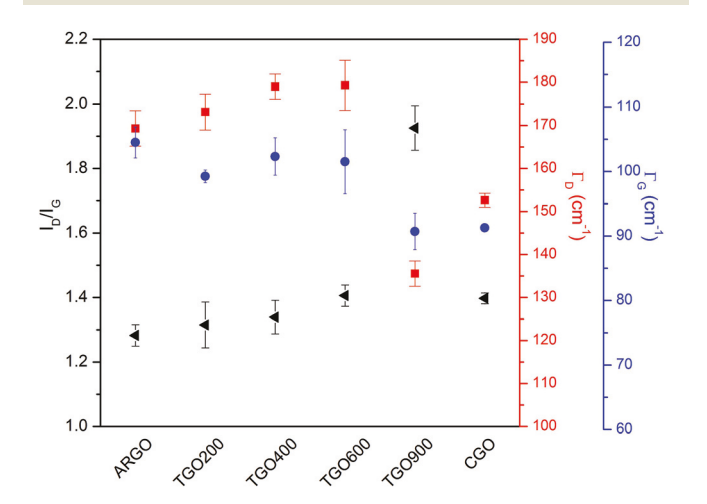


Fig. 2 Variation of the  $I_{\rm D}/I_{\rm G}$  values (black triangles), the FWHM of D band ( $\Gamma_{\rm D}$ , red squares) and the FWHM of G band ( $\Gamma_{\rm G}$ , blue circles) for ARGO, TGOs, and CGO. Triplicate measurements in different locations of each sample were carried out and the error bars represent the standard deviation of repeated measurements.

approaches result in an increase in the  $I_D/I_G$  ratio, with that of TGOs systematically increasing with increasing annealing temperature (1.28-1.92 from ARGO to TGO900). Previous studies attributed this increase in  $I_D/I_G$  of rGO to an increase in structural defects (e.g., holes) and a decrease in the average size of the sp<sup>2</sup> domain according to the Tuinstra-Koenig equation  $(I_D/I_G \propto 1/L_a)$ .  $^{54,55,61-63}$  However, there is a competing explanation of the defect-induced D band<sup>57,60,64</sup> in which the resulting  $I_D/I_G$  ratio is a function of  $L_a$  and  $L_d$ , and the  $I_D/I_G$ dependence on each is differentiated by two stages. Stage 2 is characterized by the increase in  $I_D/I_G$  with increasing  $L_d$ , up to  $L_{\rm d} \sim 3$  nm and  $L_{\rm a} \sim 2$  nm, where  $I_{\rm D}/I_{\rm G}$  reaches the maximum and signifies the boundary between stage 2 and stage 1. Stage 1 is characterized by a decreasing trend in  $I_D/I_G$  as  $L_d$  increases, defined by  $L_d > 3$  nm and  $L_a > 2$  nm (see Fig. 5 in ref. 57 and Fig. 3 in ref. 60 for further details). As a result, the increase of  $I_{\rm D}/I_{\rm G}$  can be explained by either a decrease or increase in defect density depending on mechanistic explanation and the regime to which the materials belong.

In stage 1, which is indicative of the nanocrystalline phase and referred to as the low defect density regime, the Tuinstra-Koenig relationship is valid and the increase of  $I_D/I_G$  corresponds with a decrease in  $L_a$  and  $L_d$ . Conversely, in stage 2, which represents the high defect density regime, the Tuinstra-Koenig relationship fails and the increase of  $I_D/I_G$  infers an increase in  $L_a$  and  $L_d$ . Before conducting an evaluation of the prepared GO/rGO material suite in the present study, it is important to first identify the appropriate regime (i.e., stage 2 or stage 1) by analyzing Raman spectra. The broad bump-like peak in the 2D region and the full width at half maximum (FWHM,  $\Gamma$ ) of G band ( $\Gamma_{\rm G}$ ) (~90-100 cm<sup>-1</sup>) displayed in our samples are characteristics of stage 2.  $^{59,60,65}$  Thus, the  $I_{\rm D}/I_{\rm G}$ increase with the increase in the level of reduction, from ARGO to TGOs or CGO, indicates the improvement in ordering and the formation of more defect-free sp<sup>2</sup> domains of larger size. In other words, the ARGO experiences a transformation from small sp<sup>2</sup> clusters interspersed by an amorphous and highly disordered sp<sup>3</sup> matrix to a larger sp<sup>2</sup> carbon network upon systematic reduction of oxygen function groups. In addition, while the  $\Gamma_{\mathrm{D}}$  and  $\Gamma_{\mathrm{G}}$  do not change significantly from ARGO and TGOs annealed below 900 °C, there is a significant decrease in both  $\Gamma_{\mathrm{D}}$  and  $\Gamma_{\mathrm{G}}$  for the TGO900 and CGO samples. This indicates that these reduction conditions are effective at 'healing' the GO defects. Finally, the TGO sample of comparable sp<sup>2</sup> carbon fraction to that of the CGO sample (TGO600, Table 1) has distinct  $\Gamma_{\rm D}$  and  $\Gamma_{\rm G}$ , which suggests that chemical reduction produces samples with relatively lower structural disorder than the thermal reduction.

## 3.4 Investigating the electron transfer capability of GO/rGO samples through conductivity measurements

Given that the electronic properties of CNMs are important for both electrochemical and biological activities,  $^{22-26}$  the electron transfer capability of the prepared GO and rGO is evaluated here, quantified by the sample conductivity. Further, the electrical conductivity indicates how the  $\pi$  electron network of  $\rm sp^2$ 

carbons is restored upon reduction. The functional groups and defects on the GO disrupt the conjugated graphitic structure of graphene, thus, high electrical conductivity can theoretically be achieved through the reduction of GO and restoration of the conjugated structure.<sup>63</sup> Due to the high defect density introduced by oxygen functionalization (38.70 at% O), the resistivity of ARGO approaches infinity and exceeds the full-scale value of the four-point probe unit. While ARGO is deemed an insulator, 63,66 resistivity values obtained for the rGO samples indicate a range in electron transfer capability. The corresponding conductivity of the TGO400, TGO600, TGO900, and CGO samples are 0.47, 2.59, 13.77 and 8.54 S m<sup>-1</sup>, respectively. This trend in conductivity agrees with the XPS and Raman results; an increase in rGO conductivity is represented by XPS data as a greater % sp<sup>2</sup> carbon and by Raman as lower defect density and larger sp<sup>2</sup> crystallite size. This agreement in measured conductivity by four-point probe, XPS and Raman is similarly reported by others, 33,47,63 and is rationalized by the increase in sp<sup>2</sup> carbon (XPS) and decrease in the defect density (Raman) representing the recovery of  $\pi$  conjugated structure. Further, the growth in the crystallite size (increasing  $I_D/I_G$  ratio in region 2) indicates a reduction of grain boundaries (the interface between two single crystallites, or grains, in a polycrystalline material), which have been shown to degrade the electrical property of graphene.67,68

The relative conductivity values of TGO600, TGO900 and CGO merit further discussion. CGO has a higher conductivity than TGO600 despite having a comparable % sp² carbon (Table 1) and  $I_{\rm D}/I_{\rm G}$  ratio (Fig. 2). This is attributed to the lower disorder of the CGO structure (reflected by lower  $\Gamma_{\rm D}$  and  $\Gamma_{\rm G}$  values, Fig. 2), a benefit realized through the chemical reduction method. Specifically, thermal annealing induces expansion of the graphene lattice through generation and release of CO or CO<sub>2</sub> gases, which introduces structural damage (*e.g.*, holes) in the graphene plane. <sup>30,63,69</sup> These lattice defects inevitably influence the electronic properties by interrupting electron transport and disturbing conductive path-

ways. In contrast, chemical reduction preserves the graphene structure; the reduction process is based on chemical reactions between functional groups and a reducing agent, which causes minor impacts to the structure of the carbon plane. Given that subtle enhancements in long-range conjugated structures of the sp<sup>2</sup> lattice can impart a significant conductivity enhancement, the preservation of the conjugated graphene structure through chemical reduction (compared to thermal) results in significantly higher conductivity of the CGO compared to TGOs annealed below 900 °C.

# 3.5 Biological activity changes as a function of GO/rGO physicochemical properties

Proposed mechanisms of adverse biological outcomes of graphene-based materials include membrane stress caused by physical disruption, <sup>12,70,71</sup> physical interference of essential nutrient fluxes due to diffusion limitation, 72 and induced oxidative stress via reactive oxygen species (ROS)-mediated or ROS-independent pathways. 12,13,16,73-75 Among these mechanisms, oxidative stress is cited as the dominant mechanism for graphitic nanomaterial toxicity to cells. 12,16,73 Graphene, GO and rGO can mediate cellular oxidative stress through, (i) the formation of ROS from oxygen adsorption, or (ii) by the direct binding with or oxidation of cellular biomolecules. 13,75-77 GSH is one such biomolecule that serves to maintain a healthy cellular redox environment and plays an important role in protecting against cellular oxidative stress. 12,13 The propensity for the prepared GO/rGO samples to oxidize GSH (referred to as oxidative potential) thus, serves as a metric to compare the relative biological activity in the present study.

Fig. 3 includes the compiled results presenting several important points. First, the magnitude of oxidative potential scales with GO/rGO concentration (Fig. 3a *versus* 3b). Second, and most importantly, the magnitude of GO/rGO-mediated GSH oxidation shifts for differentially treated samples. (The importance and relative contribution of surface chemistry as

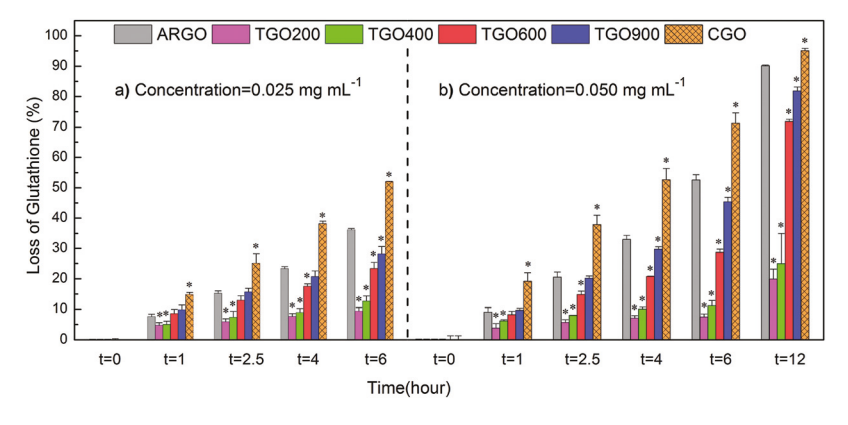


Fig. 3 Time-dependent GSH oxidation mediated by the prepared GO/rGO samples. Two mass loadings were evaluated, (a)  $0.025 \text{ mg mL}^{-1}$  and (b)  $0.050 \text{ mg mL}^{-1}$ , to demonstrate mass-dependent GSH oxidation. In addition, extended time points in (b) were included to (i) confirm eventual 100% GSH oxidation and (ii) inform subsequent kinetic analysis. Samples were run in triplicate and the error bars represent the sample standard deviation of repeated experiments. Asterisk (\*) denotes the statistically significant differences in means compared to the ARGO by two-sample t test (95% CI, P < 0.05).

**Paper** 

well as the consequential physicochemical property modifications that result from thermal and chemical reduction will be discussed in detail below with the respective characterization data.) Third, time-dependent GSH oxidation indicates, (i) the loss of GSH scales with exposure time, and (ii) suggests that the GO/rGO-GSH interaction is chemical in nature rather than proceeding through physical adsorption because the latter is typically a fast process.<sup>75</sup> As such, the oxidation of GSH by the GO/rGO is the dominant mechanism of GSH loss.

To further evaluate the kinetics of GSH oxidation, a kinetic model was applied to the collected data to estimate a kinetic rate constant, providing insight into the respective sample oxidative potential. In these calculations, it is assumed that the adsorption of reactant (GSH) and desorption of product (e.g., GSSG) from the GO/rGO surface is fast. The GO/rGO-GSH interaction is expressed with the following first-order rate law:<sup>75,78</sup>

$$-\left(\frac{\mathrm{d}[\mathrm{GSH}]}{\mathrm{d}t}\right) = k[\mathrm{GSH}][\mathrm{GO}] \to \ln[\mathrm{GSH}] = -k[\mathrm{GO}]t + C \qquad (1)$$

where k is the rate constant (mL mg<sup>-1</sup> h<sup>-1</sup>), [GSH] is the concentration of GSH remaining in solution, [GO] is the concentration of the GO/rGO sample (0.050 mg mL<sup>-1</sup>), C is a constant of this integration equation and represents the natural log of the initial concentration of GSH. By plotting ln[GSH] *versus* time (Fig. S7†), the rate constants (k) are determined from the slope of the resulting linear curve fits to be 3.39, 0.35, 0.56, 1.84, 2.57 and 4.72 mL mg<sup>-1</sup> h<sup>-1</sup> for ARGO, TGO200, TGO400, TGO600, TGO900, and CGO, respectively. Finally, there is a good fit of the data with the assumed first-order kinetic model ( $R^2 > 0.98$ ).

Combined, the results suggest that GO/rGO-mediated loss of GSH is both time and concentration dependent, and that within a given concentration, the differentially treated GO samples have different propensities for GSH oxidation, represented by their estimated rate constants, CGO > ARGO > TGO900 > TGO600 > TGO400 > TGO200. Finally, the extended time point (12 h, Fig. 3b) demonstrates that 100% loss of GSH can be achieved given sufficient interaction time. In the 0.050 mg mL $^{-1}$  system, 90% and 95% loss of GSH are achieved after 12 h exposure for ARGO and CGO, respectively.

Among the six samples, noteworthy differences in biological activity are observed. The following trends are described in turn. Primary physicochemical properties, including aggregate size, presence of defects, electrical conductivity, and surface chemistry, have been proposed as contributing factors that influence the oxidative capacity of CNMs. 12,13,19,24,75,76 No single property can explain the observed trends attained in this research, rather the relative contribution of each is discussed in the context of each noteworthy trend.

**Oxidative potential of ARGO.** ARGO exhibits a higher capacity to oxidize GSH than the thermally reduced samples. A primary difference between ARGO and TGO samples is the amount of surface oxygen and thus, greater defect density of ARGO. The high defect density on the highly-oxidized carbon

surface can facilitate adsorption of oxygen, providing the opportunity to generate ROS (e.g., peroxide, superoxide) and promote GSH oxidation.<sup>75,76</sup> In addition, surface oxygen is known to influence the dispersive properties of GO/rGO,66 and aggregation has been shown to affect the extent of GO/rGOinduced oxidative stress. 12,13 The dispersed aggregate size was estimated from the peak location of dynamic light scattering (DLS) data in which samples were prepared in the same manner as for the GSH assay. The compiled data (Fig. S8†) indicates that all samples are composed of heterogeneously dispersed aggregates (i.e., multiple peaks and/or broad peaks). Relative peak locations indicate that ARGO has the smallest overall dispersed aggregates (two peaks, both below 1 µm). The highly-oxidized surface (C/O ratio =  $1.58 \pm 0.04$ ) introduces hydrophilic properties unique to ARGO, enabling good dispersion and stability in aqueous media. Peak shifts towards larger aggregates are observed for the TGO samples corresponding with the reduction of surface oxygen. This trend is also reflected in the AFM image analysis (Fig. S2†). The enhanced dispersion of ARGO facilitates interaction with target molecules (e.g., greater available active surface area), giving rise to the enhanced oxidative potential towards GSH. Finally, the high concentration of epoxide groups is a characteristic of GO (as noted in the XPS discussion) and the high steric strain of epoxides introduces reactive surface sites, further enhancing the oxidative potential of ARGO. The thiol group of GSH may serve as the nucleophile attacking the electrophilic carbon atom of the epoxide group facilitating a ringopening reaction.<sup>79</sup> This process also contributes to the loss (or oxidation) of GSH. Given the thermal lability of epoxides, the relative concentration on the surface of GO is significantly reduced upon thermal annealing. Therefore, this additional mechanism of GSH oxidation is only present for the ARGO sample.

Oxidative potential of rGO samples correlates with conductivity and the presence of carbonyl moieties. The loss of GSH systematically increases with maximum annealing temperature from 200-900 °C and is significantly greater for the CGO sample. The factors identified to contribute to the enhancement of ARGO oxidative potential are weakly correlated, at best, with the observed trend of rGO samples (i.e., the defect density decreases, the aggregate size becomes larger and the quantity of epoxide groups decreases upon thermal and chemical reduction). Therefore, for the observed trend is GSH oxidation must result from other rGO properties. As previously discussed, the conductivity of the rGO samples increases with systematic reduction in surface oxygen groups. High conductivity of rGO will accelerate the electron transfer necessary to mediate the oxidation reaction of GSH. However, the TGO900 has the highest measured conductivity, yet CGO has the highest oxidative potential. This suggests that another factor is involved in the observed biological activity. The relative presence of carbonyl moieties on the surface of CNMs has been shown to play an important role in facilitating the oxidation of GSH. 19,24 The presence of C=O groups differs for these samples with a greater relative presence in the CGO

sample (3.21% in TGO900 and 5.50% in CGO, Table 1), suggesting that both conductivity and carbonyl moieties play an important role in the biological activity of rGO samples.

Combined, the results suggest that GSH oxidation mediated by GO/rGO samples is not controlled by a sole-factor, but instead, is governed by the synergetic effects of consequential properties, including dispersed aggregate size, defect density, electrical conductivity, and the relative presence of carbonyl moiety.

#### 3.6 Electrochemical activity of the prepared GO/rGO samples

The realization that CNMs can promote the oxygen reduction reaction (ORR) has inspired their use in energy conversion and storage such as fuel cells and metal-air batteries. <sup>9,80</sup> Electrochemical performance (*i.e.*, facilitating the rate of electron transfer) of a material is commonly measured *via* the ORR and represents the propensity of a material to promote or catalyze the reduction of oxygen. Thus, ORR was used here to examine and compare the electrochemical activity of the prepared GO/rGO material suite.

Previous research on O-MWCNTs demonstrates a significant correlation between biological and electrochemical activities. <sup>19,24</sup> In that work, the enhanced activity was attributed to the ability of differentially treated O-MWCNTs to facilitate the exchange of electrons necessary for both GSH oxidation and ORR. Due to this established connection between GSH oxidation and ORR, both activities were studied here to identify if the same conclusions are transferable across CNM classes. The electrochemical activities of ARGO, TGOs, and CGO were investigated by ORR experiments (in the alkaline media) using the RRDE technique. The evaluation of electrochemical performance using RRDE provides insight into the electrocatalytic activity and electron transfer kinetics of the prepared GO/rGO samples.

The polarization curves for all samples are compiled in Fig. 4 (1600 rpm, oxygen saturated 1 M KOH solution). A summary of the electrochemical activity indicators determined from this data, including the half-wave potential  $(E_{1/2})$ , the onset potential, the limiting current  $(J_L)$  and the electroactive surface area (A), is presented in Table 2.  $E_{1/2}$ , onset potential, and  $J_{\rm L}$  were acquired from polarization curves in Fig. 4, and A was obtained from CV curves (Fig. S10†). The kinetic limiting current density  $(J_K)$ , which indicates the intrinsic ORR activity by excluding the mass transport limited component of oxygen adsorption kinetics, was calculated from the corresponding Koutecky-Levich (K-L) plots (Fig. S11†) and is included in Fig. S12.† Enhancement in electrochemical activity is represented by a greater absolute value of the current density and limiting current, a more positive  $E_{1/2}$ , and a more positive onset potential.

Identifying trends in ORR activity of GO and rGO. Similar to the relative biological activity discussed above, ARGO presents unique electrochemical properties. While a more positive  $E_{1/2}$  and onset potential indicate more favorable ORR activity for ARGO compared to the TGO samples, the electrocatalytic activity of ARGO is significantly lower, as indicated by the  $J_{\rm L}$ 

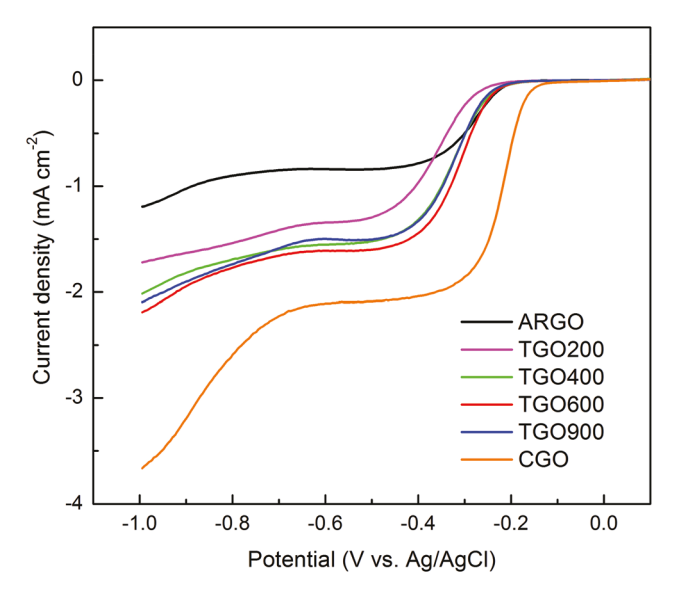


Fig. 4 ORR polarization curves of ARGO, TGOs, and CGO in  $O_2$ -saturated 1 M KOH solution with 1600 rpm rotating speed. All curves display a feature of two regions separated at the potential around -0.5 V, the lower overpotential region is indicative of the reduction of  $O_2$  to  $HO_2^-$ , and the higher overpotential region for the reduction of  $HO_2^-$  to  $H_2O$ . The half-wave potential ( $E_{1/2}$ ), the onset potential, and the limiting current density ( $J_1$ ) were determined by analyzing the polarization curve in the first region, wherein the onset potential was determined from the intersection of the tangents between the baseline and the current signal.

and  $J_{\rm K}$  values, representing a lower density of active sites toward ORR at higher overpotentials. Among the TGO samples, an increase in the electrocatalytic activity is observed with the increase of the annealing temperature until 600 °C, followed by a notable decrease for the TGO900. This trend is reflected in all the indicators ( $E_{1/2}$ , onset potential,  $J_L$ , and  $J_K$ ). It is interesting to note the improved electrocatalytic activity in the CGO, particularly in terms of the  $E_{1/2}$ , onset potential and current density. The  $J_K$  values of CGO at two representative potentials, -0.45 V and -0.75 V, is significantly greater than those of ARGO and TGOs. Finally, the trend in electroactive surface area, estimated by the Randles-Sevcik equation, agrees well with that of the other discussed electrochemical metrics (see Table 2). Specifically, CGO has the greatest electrocatalytic surface area (0.2808 cm<sup>2</sup>) and that of TGO600 (0.1922 cm<sup>2</sup>) is the greatest among the TGO samples. This indicates that the manipulation of the ARGO under these conditions leads to the increase in the active sites and further enhances the current density.

To gain insight into the ORR pathway, as the 2-electron or direct 4-electron reduction,  $^{81}$  the electron transfer number (n) and concentration of produced  $H_2O_2$  were obtained from RRDE experiments (Fig. S13, including detailed discussion in the ESI† on the determination of n). The number of electrons transferred remains greater than 3.2 over the range of potentials for all GO/rGO samples, indicating the contribution of the more efficient 4-electron pathway. The production of  $H_2O_2$ 

Table 2 Electrochemical indicators used to evaluate the ORR performance, including the half-wave potential ( $E_{1/2}$ ), the onset potential, the limiting current density ( $J_L$ ), the kinetic limiting current density ( $J_K$ ), and the electroactive surface area (A). In general, an enhancement in ORR performance is represented by the higher  $J_L$  and  $J_K$ , the higher A, more positive  $E_{1/2}$  and a more positive onset potential

Samples	$E_{1/2}^{a}(V)$	Onset potential <sup>a</sup> (V)	$J_{ m L}^{a}$ (mA cm $^{-2}$ )	$J_{\rm K}^{\ \ b}$ (mA cm <sup>-2</sup> , -0.45 V)	$J_{\rm K}^{\ \ b}$ (mA cm <sup>-2</sup> , -0.75 V)	$A^{c}$ (cm <sup>2</sup> )
ARGO	-0.2862	-0.2143	-0.8408	1.9283	1.9331	0.0230
TGO200	-0.3590	-0.2744	-1.3395	2.6364	4.8996	0.0957
TGO400	-0.3258	-0.2445	-1.5471	4.5188	6.3816	0.1481
TGO600	-0.3127	-0.2344	-1.6101	6.9735	9.4429	0.1922
TGO900	-0.3226	-0.2445	-1.5075	5.6818	9.1491	0.1771
CGO	-0.2201	-0.1695	-2.0885	25.9067	26.1097	0.2808

<sup>&</sup>lt;sup>a</sup> Data extracted from Fig. 4. <sup>b</sup> Data extracted from Fig. S12 (the values of  $J_{\rm K}$  were tabulated at two representative potentials from the low and high potential regions, respectively). <sup>c</sup> Data extracted from Fig. S10.

during ORR is commonly monitored in fuel cell research as the presence of  $\rm H_2O_2$  can degrade the catalyst layer and lower the utilization of oxygen. <sup>82</sup> As such, the observed low  $\rm H_2O_2$  yield (<15%) and high electron transfer number (>3.6) for the CGO sample suggests it is a more effective catalyst towards ORR. Note that the goal of this study is not to develop the optimal catalysts, rather to utilize the standard metrics and interpretation of the trends in data to probe the role of surface chemistry manipulations on  $\rm GO/rGO$  electrochemical activity.

Considering the data from both the GSH oxidation and ORR experiments, different trends were observed for the GO/ rGO samples. In the ORR experiments, the electrochemical activity decreases as: CGO > TGO600 > TGO900 > TGO400 > TGO200 > ARGO. Most notably, ARGO has relatively high capacity to oxidize GSH but has the lowest ORR activity, and a modest decrease of electrochemical activity is observed in TGO900 compared to TGO600. As such, the trends in the biological and electrochemical activities of GO/rGO samples are not synchronous as previously observed for O-MWCNTs, 19,24 indicating that surface chemistry alone cannot elucidate the observed trends in the current study of GO/rGO materials. Several factors have been associated with superior ORR performance of graphene-based materials, including (i) good electrical conductivity of materials to transfer electrons between the active catalytic sites, 83-85 (ii) edge defects (e.g., holeinduced edges, edge-plane-like sites, and dangling bonds) and topological defects (e.g., pentagons and heptagons - five- and seven-carbon rings, respectively) introduced during the reduction processes that serve as electroactive sites for ORR, 69,86 (iii) high electroactive surface area indicative of more active sites accessible to ORR,85 and (iv) the presence of active functional groups (e.g., quinone groups, C=O) on the carbon surface that are known to enhance the electrocatalysis of oxygen reduction through the production of the semiquinone radicals that accelerate the rate of electron transfer. 24,87,88 The relative role of each factor in the observed ORR activity will be discussed further.

The relative importance of conductivity and defects in the electrochemical activity. As postulated by the widely accepted Lerf–Klinowski model, large amounts of hydroxyl and epoxide groups are located mainly within basal planes, with a lower

amount of C=O and COOH species on the outer edges of GO. <sup>89,90</sup> During the reduction process, edge-planes are progressively exposed as C=O and COOH groups are reduced. In addition, defects within the basal plane are introduced in the form of hole-induced edges as well as topological defects like pentagon and heptagons. <sup>69,86</sup> These defect sites on both the edge and basal planes have demonstrated strong electrocatalytic activity and can be effective active sites for the ORR by means of redistributing the local electron density and enhancing the affinity to the intermediates. <sup>87,91–94</sup> Likewise, the dangling bonds at the edges are reactive edge defects and can be effective O<sub>2</sub> adsorption sites. <sup>95</sup>

While both conductivity and defects (at the edge and in basal plane) influence the electrochemical activity, it is proposed that conductivity is the dominant factor as evidenced here by the CGO sample. First, the CGO sample has fewer defects within the basal plane due to the inherent difference in the reduction methods, namely the chemical reduction method preserves the graphene basal plane (vide supra). Second, CGO has a higher fraction of edge-plane groups (i.e., C=O and COOH) than TGO600 (Table 1) – the sample with the next highest electrochemical activity – indicating there are fewer exposed edge-plane defects. Therefore, the prominent contribution of the material conductivity to the ORR activity of CGO is rationalized by the fact that the sample has fewer ORR-active defect sites and significantly enhanced electrocatalytic performance.

Synergistic contributions of conductivity and the carbonyl moiety to enhanced electrochemical activity. The important role of carbonyl groups in the electrochemical activity of GO/rGO materials is demonstrated through the comparison of TGO600, TGO900 and CGO. The conductivity of TGO900 is significantly higher than TGO600 and CGO, yet the electrochemical performance of TGO900 is inferior to these other two samples. Interestingly, TGO900 has a lower relative proportion of C=O moieties compared with the TGO600 and CGO samples (Table 1). Taken together, the data highlights the important contributions of electrical conductivity and carbonyl moieties to enhancement of electrochemical activity. To delineate the influence of electrical conductivity and carbonyl moieties, the conductivity is plotted against the percentage of car-

Published on 23 March 2017. Downloaded by University of Pittsburgh on 7/18/2018 2:18:08 AM

**Green Chemistry** 

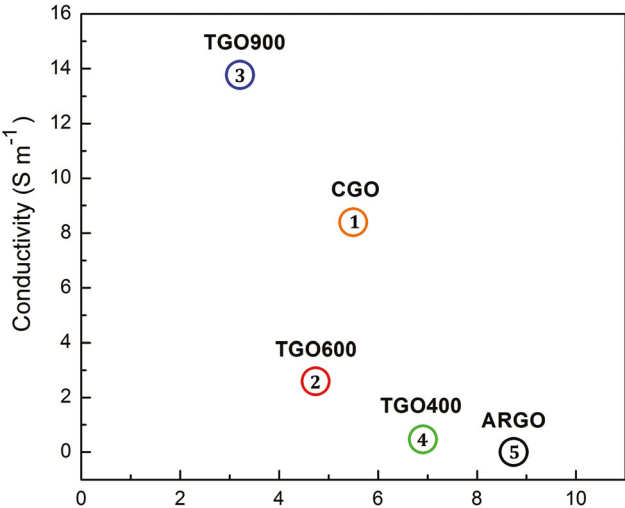


Fig. 5 The enhancement of electrochemical activity as a function of two critical contributing factors: electrical conductivity and the percentage of carbonyl moiety (% C=O). The conductivity of ARGO is assumed to be zero based on observed insulating behavior during four-point probe measurements. The numeric numbers from 1 through 5 refer to the order of electrochemical activity with 1 as the maximum and 5 as the minimum

C=O (%)

bonyl moiety (% C=O). In Fig. 5, the bottom-left (low conductivity and low % C=O) is the most unfavorable region while the top left (high conductivity and low % C=O) and bottom right (low conductivity and high % C=O) present deficiencies in one of the two contributing factors - carbonyl moieties and conductivity, respectively. The top-right (high conductivity and high % C=O) is theoretically limited, given that the inclusion of surface functionalities inherently disrupts the long-range ballistic transport of graphene materials. The optimal electrochemical activity is achieved with a balance of the conductivity and % C=O, and confirmed empirically by the CGO and TGO600 samples.

#### Conclusions

The results presented from the systematically treated and comprehensively characterized GO/rGO material suite reveal that the previously established correlation for O-MWCNTs between, (i) electrochemical and biological activities, and (ii) the relative presence of carbonyl-containing moieties, is not wholly maintained. Rather, changes in properties as a consequence of modulating surface chemistry play an important role in governing biological and electrochemical activity of GO/rGO materials. Taken together, the results suggest that both activities are driven by synergistic effects from multiple factors informing the following conclusions:

(i) Dispersed aggregate size and defect density (particularly the presence of reactive groups like epoxides) are the primary properties that influence the biological activity of highly oxidized graphene, as demonstrated by the ARGO sample. Yet, when dispersion is eliminated as a factor, such is the case with electrochemical measurements where the material is deposited on an electrode, the highly-oxidized surface does not contribute favorably to this functional performance.

- (ii) Restoration of the long-range conjugated graphitic structure, achieved through both thermal and chemical reduction approaches, enhances rGO electrical conductivity contributing to increased oxidation of GSH. A noticeable effect of the carbonyl moiety on the GSH oxidation also emerges as a contributing property as demonstrated by the comparison of TGO900 and CGO samples.
- (iii) Electrical conductivity and the presence of carbonyl moieties both contribute to enhanced electrochemical activity, which can be optimized through a balance of these two properties, as demonstrated through the TGO600 and CGO samples.

Combined, these findings indicate that surface chemistry is a viable design handle to effectively control biological and electrochemical activity of rGO materials. Yet, rather than a single property modulating function and hazard, it is the balance of two synergistic properties that can be manipulated to control function and hazard. In this way, the addition of a dimension to previously established structure-property-function (SPF) and structure-property-hazard (SPH) plots<sup>23</sup> is proposed in Fig. 6 for a subset of rGO samples (TGO400, TGO600, TGO900, and CGO). Still, enhancement of the desired function (here, electrochemical activity) is concomitant with enhancement of inherent materials hazard (here, biological activity measured as the oxidation of GSH).

The ultimate goal sought through this and ongoing research endeavors is the ability to tailor function and hazard

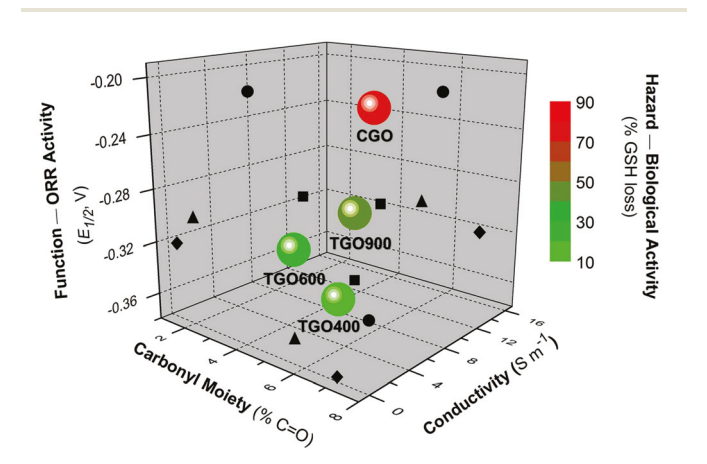


Fig. 6 Structure-property-function (SPF) and structure-propertyhazard (SPH) parametric plot for the rGO sample set, including two synergistic materials properties – conductivity (S m<sup>-1</sup>) and the presence of carbonyl moieties (% C=O). The function - ORR activity - is represented by the half-wave potential,  $E_{1/2}$  (V), and the hazard – biological activity - is represented by the percent loss of GSH (after 6 h exposure to 0.050 mg mL<sup>-1</sup> rGO samples). Each sphere is an independent rGO sample. The symbols indicate data projections for each sample onto the three planes: rhombuses (♠, TGO400), triangles (▲, TGO600), squares (■, TGO900), and circles (●, CGO).

**Paper** 

properties in a controllable and independent manner. Yet, it is possible that electrochemical activity and the propensity to induce biological oxidative stress are inextricably linked given the underlying mechanisms of GSH and ORR require an exchange of electrons (facilitated here by the CNMs). Still, there remains the opportunity to further evaluate the rational design of CNMs and the potential to decouple these activities through surface chemistry manipulations by investigating additional (non-oxygen) functional groups (e.g., other heteroatom doping). In doing so, the contribution of carbonyl-containing groups is eliminated. Heteroatoms, such as nitrogen, sulfur, and boron, have demonstrated favorable influence on the electrochemical activity and conductivity, 37,38,96-100 providing an avenue to control these two factors. While the biological activity of nitrogen-doped or functionalized CNTs has not been comprehensively studied, there is an indication of lower toxicity. 101 Through the holistic and systematic approach described herein, the underlying mechanisms of CNM activity will be elucidated to inform a guiding framework for rational and sustainable design of CNMs.

## Acknowledgements

The authors acknowledge generous support from the Department of Civil and Environmental Engineering and Swanson School of Engineering at the University of Pittsburgh. The facilities in the Gertrude E. and John M. Petersen Institute of NanoScience and Engineering (PINSE) and the Materials Characterization Laboratory (MCL) at the University of Pittsburgh were utilized for material characterization. The authors would also like to thank their colleagues, Dr Joel Gillespie for assistance with XPS, Raman, and AFM measurements, Dr Howard Fairbrother for helpful discussions on XPS peak deconvolution, Dr Francois Perreault for useful advice on AFM sample preparation, Dr Paul Leu for helpful insight on conductivity measurements, and Amey More for assistance with TGA measurements.

#### Notes and references

- 1 P. Anastas and N. Eghbali, *Chem. Soc. Rev.*, 2010, **39**, 301–312.
- 2 P. T. Anastas and M. M. Kirchhoff, Acc. Chem. Res., 2002, 35, 686–694.
- 3 J. Kostal, A. Voutchkova-Kostal, P. T. Anastas and J. B. Zimmerman, *Proc. Natl. Acad. Sci. U. S. A.*, 2015, **112**, 6289–6294.
- 4 K. A. Connors, A. M. Voutchkova-Kostal, J. Kostal, P. Anastas, J. B. Zimmerman and B. W. Brooks, *Environ. Toxicol. Chem.*, 2014, 33, 1894–1902.
- 5 A. McWilliams, BCC Research, NAN031G, 2016.
- 6 D. Jariwala, V. K. Sangwan, L. J. Lauhon, T. J. Marks and M. C. Hersam, *Chem. Soc. Rev.*, 2013, 42, 2824–2860.

- 7 W. Yang, K. R. Ratinac, S. P. Ringer, P. Thordarson, J. J. Gooding and F. Braet, *Angew. Chem., Int. Ed.*, 2010, 49, 2114–2138.
- 8 M. J. Allen, V. C. Tung and R. B. Kaner, *Chem. Rev.*, 2010, 110, 132–145.
- 9 Y. Shao, J. Wang, M. Engelhard, C. Wang and Y. Lin, J. Mater. Chem., 2010, 20, 743-748.
- 10 J. Hou, Y. Shao, M. W. Ellis, R. B. Moore and B. Yi, *Phys. Chem. Chem. Phys.*, 2011, 13, 15384–15402.
- 11 M. F. De Volder, S. H. Tawfick, R. H. Baughman and A. J. Hart, *Science*, 2013, 339, 535–539.
- 12 S. Liu, T. H. Zeng, M. Hofmann, E. Burcombe, J. Wei, R. Jiang, J. Kong and Y. Chen, *ACS Nano*, 2011, 5, 6971– 6980.
- 13 F. Perreault, A. F. de Faria, S. Nejati and M. Elimelech, ACS Nano, 2015, 9, 7226–7236.
- 14 O. Akhavan and E. Ghaderi, ACS Nano, 2010, 4, 5731–5736.
- 15 X. Zhao and R. Liu, Environ. Int., 2012, 40, 244-255.
- 16 L. Chen, P. Hu, L. Zhang, S. Huang, L. Luo and C. Huang, *Sci. China: Chem.*, 2012, 55, 2209–2216.
- 17 X. T. Liu, X. Y. Mu, X. L. Wu, L. X. Meng, W. B. Guan, Y. Q. Ma, H. Sun, C. J. Wang and X. F. Li, *Biomed. Environ.* Sci., 2014, 27, 676–683.
- 18 E. L. K. Chng and M. Pumera, Chem. Eur. J., 2013, 19, 8227–8235.
- 19 L. M. Pasquini, R. C. Sekol, A. D. Taylor, L. D. Pfefferle and J. B. Zimmerman, *Environ. Sci. Technol.*, 2013, 47, 8775–8783.
- 20 E. J. Petersen, L. Zhang, N. T. Mattison, D. M. O'Carroll, A. J. Whelton, N. Uddin, T. Nguyen, Q. Huang, T. B. Henry, R. D. Holbrook and K. L. Chen, *Environ. Sci. Technol.*, 2011, 45, 9837–9856.
- 21 X. Hu and Q. Zhou, *Chem. Rev.*, 2013, **113**, 3815–3835.
- 22 A. B. Seabra, A. J. Paula, R. de Lima, O. L. Alves and N. Durán, *Chem. Res. Toxicol.*, 2014, 27, 159–168.
- 23 L. M. Gilbertson, J. B. Zimmerman, D. L. Plata, J. E. Hutchison and P. T. Anastas, *Chem. Soc. Rev.*, 2015, 44, 5758–5777.
- 24 L. M. Gilbertson, D. G. Goodwin Jr., A. D. Taylor, L. Pfefferle and J. B. Zimmerman, *Environ. Sci. Technol.*, 2014, 48, 5938–5945.
- 25 J. Wang, S. Yang, D. Guo, P. Yu, D. Li, J. Ye and L. Mao, *Electrochem. Commun.*, 2009, 11, 1892–1895.
- 26 B. Yuan, X. Zeng, C. Xu, L. Liu, Y. Ma, D. Zhang and Y. Fan, *Sens. Actuators, B*, 2013, **184**, 15–20.
- 27 N. Kurantowicz, E. Sawosz, S. Jaworski, M. Kutwin, B. Strojny, M. Wierzbicki, J. Szeliga, A. Hotowy, L. Lipińska and R. Koziński, *Nanoscale Res. Lett.*, 2015, 10, 1–12.
- 28 A. C. Neto, F. Guinea, N. M. Peres, K. S. Novoselov and A. K. Geim, *Rev. Mod. Phys.*, 2009, **81**, 109.
- 29 L. R. De Jesus, R. V. Dennis, S. W. Depner, C. Jaye, D. A. Fischer and S. Banerjee, *J. Phys. Chem. Lett.*, 2013, 4, 3144–3151.

- 31 K. P. Loh, Q. Bao, G. Eda and M. Chhowalla, *Nat. Chem.*, 2010, 2, 1015–1024.
- 32 T. Kavinkumar, D. Sastikumar and S. Manivannan, *RSC Adv.*, 2015, **5**, 10816–10825.
- 33 D. Chen, H. Feng and J. Li, *Chem. Rev.*, 2012, **112**, 6027–6053.
- 34 X. Li, H. Wang, J. T. Robinson, H. Sanchez, G. Diankov and H. Dai, *J. Am. Chem. Soc.*, 2009, **131**, 15939–15944.
- 35 W. Gao, L. B. Alemany, L. Ci and P. M. Ajayan, *Nat. Chem.*, 2009, 1, 403–408.
- 36 H. J. Shin, K. K. Kim, A. Benayad, S. M. Yoon, H. K. Park, I. S. Jung, M. H. Jin, H. K. Jeong, J. M. Kim and J. Y. Choi, *Adv. Funct. Mater.*, 2009, 19, 1987–1992.
- 37 L. Yang, S. Jiang, Y. Zhao, L. Zhu, S. Chen, X. Wang, Q. Wu, J. Ma, Y. Ma and Z. Hu, *Angew. Chem.*, *Int. Ed.*, 2011, 123, 7270–7273.
- 38 Z.-H. Sheng, H.-L. Gao, W.-J. Bao, F.-B. Wang and X.-H. Xia, *J. Mater. Chem.*, 2012, 22, 390–395.
- 39 C. D. Vecitis, K. R. Zodrow, S. Kang and M. Elimelech, ACS Nano, 2010, 4, 5471–5479.
- 40 G. Eda, G. Fanchini and M. Chhowalla, *Nat. Nanotechnol.*, 2008, 3, 270–274.
- 41 H. A. Becerril, J. Mao, Z. Liu, R. M. Stoltenberg, Z. Bao and Y. Chen, *ACS Nano*, 2008, 2, 463–470.
- 42 S. Stankovich, D. A. Dikin, R. D. Piner, K. A. Kohlhaas, A. Kleinhammes, Y. Jia, Y. Wu, S. T. Nguyen and R. S. Ruoff, *Carbon*, 2007, 45, 1558–1565.
- 43 E. Antolini, Appl. Catal., B, 2012, 123, 52-68.
- 44 S. Some, Y. Kim, Y. Yoon, H. Yoo, S. Lee, Y. Park and H. Lee, *Sci. Rep.*, 2013, 3, 1929.
- 45 J. I. Paredes, S. Villar-Rodil, A. Martínez-Alonso and J. M. D. Tascón, *Langmuir*, 2008, 24, 10560–10564.
- 46 D. Lee and J. Seo, J. Phys. Chem. C, 2011, 115, 2705-2708.
- 47 C. Mattevi, G. Eda, S. Agnoli, S. Miller, K. A. Mkhoyan, O. Celik, D. Mastrogiovanni, G. Granozzi, E. Garfunkel and M. Chhowalla, *Adv. Funct. Mater.*, 2009, **19**, 2577–2583.
- 48 D. Yang, A. Velamakanni, G. Bozoklu, S. Park, M. Stoller, R. D. Piner, S. Stankovich, I. Jung, D. A. Field, C. A. Ventrice Jr. and R. S. Ruoff, *Carbon*, 2009, 47, 145– 152.
- 49 W.-C. Hou, I. Chowdhury, D. G. Goodwin Jr., W. M. Henderson, D. H. Fairbrother, D. Bouchard and R. G. Zepp, *Environ. Sci. Technol.*, 2015, 49, 3435–3443.
- 50 J. Robertson and E. P. O'Reilly, *Phys. Rev. B: Condens. Matter*, 1987, 35, 2946–2957.
- 51 Y. Jiang, R. Raliya, J. D. Fortner and P. Biswas, *Environ. Sci. Technol.*, 2016, **50**, 6964–6973.
- 52 R. Rozada, J. I. Paredes, S. Villar-Rodil, A. Martínez-Alonso and J. M. Tascón, *Nano Res.*, 2013, **6**, 216–233.
- 53 R. Beams, L. G. Cançado and L. Novotny, *J. Phys.: Condens. Matter*, 2015, 27, 083002.
- 54 M. Singh, A. Yadav, S. Kumar and P. Agarwal, *Appl. Surf. Sci.*, 2015, **326**, 236–242.

- 55 K. Krishnamoorthy, M. Veerapandian, K. Yun and S. J. Kim, *Carbon*, 2013, 53, 38–49.
- 56 A. Kaniyoor and S. Ramaprabhu, AIP Adv., 2012, 2, 032183.
- 57 A. C. Ferrari and J. Robertson, *Phys. Rev. B: Condens. Matter*, 2000, **61**, 14095.
- 58 S. Claramunt, A. Varea, D. López-Díaz, M. M. Velázquez, A. Cornet and A. Cirera, *J. Phys. Chem. C*, 2015, **119**, 10123–10129.
- 59 S. Eigler, C. Dotzer and A. Hirsch, *Carbon*, 2012, **50**, 3666–3673.
- 60 L. G. Cançado, A. Jorio, E. M. Ferreira, F. Stavale, C. Achete, R. Capaz, M. Moutinho, A. Lombardo, T. Kulmala and A. Ferrari, *Nano Lett.*, 2011, 11, 3190– 3196
- 61 D.-T. Phan and G.-S. Chung, Effects of oxygen-functional groups on humidity sensor based graphene oxide thin films, in *Sensors*, *2012 IEEE*, IEEE, 2012, pp. 1–4.
- 62 Z. Bo, X. Shuai, S. Mao, H. Yang, J. Qian, J. Chen, J. Yan and K. Cen, *Sci. Rep.*, 2014, **4**, 4684.
- 63 S. Pei and H.-M. Cheng, Carbon, 2012, 50, 3210-3228.
- 64 M. M. Lucchese, F. Stavale, E. M. Ferreira, C. Vilani, M. Moutinho, R. B. Capaz, C. Achete and A. Jorio, *Carbon*, 2010, 48, 1592–1597.
- 65 I. Jung, D. A. Dikin, R. D. Piner and R. S. Ruoff, *Nano Lett.*, 2008, **8**, 4283–4287.
- 66 D. R. Dreyer, S. Park, C. W. Bielawski and R. S. Ruoff, *Chem. Soc. Rev.*, 2010, **39**, 228–240.
- 67 W. Wu, Q. Yu, P. Peng, Z. Liu, J. Bao and S.-S. Pei, Nanotechnology, 2011, 23, 035603.
- 68 J. Červenka and C. Flipse, Phys. Rev. B: Condens. Matter, 2009, 79, 195429.
- 69 A. Bagri, C. Mattevi, M. Acik, Y. J. Chabal, M. Chhowalla and V. B. Shenoy, *Nat. Chem.*, 2010, 2, 581–587.
- 70 C. Wu, C. Wang, J. Zheng, C. Luo, Y. Li, S. Guo and J. Zhang, ACS Nano, 2015, 9, 7913–7924.
- 71 Y. Tu, M. Lv, P. Xiu, T. Huynh, M. Zhang, M. Castelli, Z. Liu, Q. Huang, C. Fan, H. Fang and R. Zhou, *Nat. Nanotechnol.*, 2013, 8, 594–601.
- 72 C. Hu, Q. Wang, H. Zhao, L. Wang, S. Guo and X. Li, *Chemosphere*, 2015, **128**, 184–190.
- 73 Y. Chang, S.-T. Yang, J.-H. Liu, E. Dong, Y. Wang, A. Cao, Y. Liu and H. Wang, *Toxicol. Lett.*, 2011, **200**, 201–210.
- 74 F. Perreault, A. Fonseca de Faria and M. Elimelech, *Chem. Soc. Rev.*, 2015, 44, 5861–5896.
- 75 X. Liu, S. Sen, J. Liu, I. Kulaots, D. Geohegan, A. Kane, A. A. Puretzky, C. M. Rouleau, K. L. More and G. T. R. Palmore, Small, 2011, 7, 2775–2785.
- 76 S. Gurunathan, J. W. Han, A. A. Dayem, V. Eppakayala and J.-H. Kim, *Int. J. Nanomed.*, 2012, 7, 5901–5914.
- 77 K. Yang, Y. Li, X. Tan, R. Peng and Z. Liu, *Small*, 2013, **9**, 1492–1503.
- 78 L. M. Gilbertson, E. M. Albalghiti, Z. S. Fishman, F. Perreault, C. Corredor, J. D. Posner, M. Elimelech, L. D. Pfefferle and J. B. Zimmerman, *Environ. Sci. Technol.*, 2016, 50, 3975–3984.

- 79 H. R. Thomas, A. J. Marsden, M. Walker, N. R. Wilson and J. P. Rourke, *Angew. Chem., Int. Ed.*, 2014, 53, 7613– 7618.
- 80 Y. Shao, J. Liu, Y. Wang and Y. Lin, *J. Mater. Chem.*, 2008, **19**, 46–59.
- 81 C. Song and J. Zhang, Electrocatalytic oxygen reduction reaction, in *PEM fuel cell electrocatalysts and catalyst layers*, Springer, 2008, pp. 89–134.
- 82 G. A. Ferrero, K. Preuss, A. Marinovic, A. B. Jorge, N. Mansor, D. J. L. Brett, A. B. Fuertes, M. Sevilla and M.-M. Titirici, ACS Nano, 2016, 10, 5922–5932.
- 83 R. Zhou, Y. Zheng, D. Hulicova-Jurcakova and S. Z. Qiao, J. Mater. Chem. A, 2013, 1, 13179–13185.
- 84 Y. Liang, Y. Li, H. Wang, J. Zhou, J. Wang, T. Regier and H. Dai, *Nat. Mater.*, 2011, **10**, 780–786.
- 85 Z.-J. Jiang and Z. Jiang, Sci. Rep., 2016, 6, 27081.
- 86 C. Gómez-Navarro, J. C. Meyer, R. S. Sundaram, A. Chuvilin, S. Kurasch, M. Burghard, K. Kern and U. Kaiser, *Nano Lett.*, 2010, 10, 1144–1148.
- 87 A. F. Holloway, G. G. Wildgoose, R. G. Compton, L. Shao and M. L. Green, *J. Solid State Electrochem.*, 2008, 12, 1337–1348.
- 88 K. Tammeveski, K. Kontturi, R. J. Nichols, R. J. Potter and D. J. Schiffrin, *J. Electroanal. Chem.*, 2001, 515, 101–112.
- 89 L. R. De Jesus, R. V. Dennis, S. W. Depner, C. Jaye, D. A. Fischer and S. Banerjee, *J. Phys. Chem. Lett.*, 2013, 4, 3144–3151.

- A. Ganguly, S. Sharma, P. Papakonstantinou and J. Hamilton, J. Phys. Chem. C, 2011, 115, 17009–17019.
- 91 C. Tang, H. F. Wang, X. Chen, B. Q. Li, T. Z. Hou, B. Zhang, Q. Zhang, M. M. Titirici and F. Wei, *Adv. Mater.*, 2016, 28, 6845–6851.
- 92 L. Tao, Q. Wang, S. Dou, Z. Ma, J. Huo, S. Wang and L. Dai, *Chem. Commun.*, 2016, 52, 2764–2767.
- 93 Y. Jiang, L. Yang, T. Sun, J. Zhao, Z. Lyu, O. Zhuo, X. Wang, Q. Wu, J. Ma and Z. Hu, ACS Catal., 2015, 5, 6707–6712.
- 94 W. Yuan, Y. Zhou, Y. Li, C. Li, H. Peng, J. Zhang, Z. Liu, L. Dai and G. Shi, *Sci. Rep.*, 2013, 3, 2248.
- 95 M. Acik and Y. J. Chabal, Jpn. J. Appl. Phys., 2011, 50, 070101.
- 96 Z. Yang, Z. Yao, G. Li, G. Fang, H. Nie, Z. Liu, X. Zhou, X. a. Chen and S. Huang, *ACS Nano*, 2011, **6**, 205–211.
- 97 Z. Chen, D. Higgins and Z. Chen, *Carbon*, 2010, 48, 3057–3065.
- 98 L. Qu, Y. Liu, J.-B. Baek and L. Dai, *ACS Nano*, 2010, 4, 1321–1326.
- 99 H. Wang, T. Maiyalagan and X. Wang, *ACS Catal.*, 2012, 2, 781–794.
- 100 K. Gong, F. Du, Z. Xia, M. Durstock and L. Dai, *Science*, 2009, 323, 760-764.
- 101 J. Carrero-Sanchez, A. Elias, R. Mancilla, G. Arrellin, H. Terrones, J. Laclette and M. Terrones, *Nano Lett.*, 2006, 6, 1609–1616.